

# Common-path interferometric detection of protein monolayer on the BioCD

Xuefeng Wang, Ming Zhao, and D. D. Nolte\*

Department of Physics, Purdue University, 525 Northwestern Avenue, West Lafayette, Indiana 47907-2036, USA

\*Corresponding author: nolte@physics.purdue.edu

Received 8 June 2007; revised 29 August 2007; accepted 31 August 2007;  
posted 7 September 2007 (Doc. ID 83945); published 2 November 2007

The bio-optical compact disk (BioCD) is an optical biosensor that performs common-path molecular interferometry of patterned proteins on a disk spinning at high speed. The common-path configuration makes it ultrastable and allows surface height precision below 10 pm. In this paper we show that two complementary interferometric quadrature conditions exist simultaneously that convert the modulus and phase of the reflection coefficient, modulated by protein patterns on the disk surface, into intensity modulation at the detector. In the far field they separate into spatially symmetric and antisymmetric intensity modulation in response to the local distribution of protein. The antisymmetric response is equivalent to differential phase-contrast detection, and the symmetric response is equivalent to in-line (IL) common-path interferometry. We measure the relative sensitivities of these orthogonal channels to printed protein patterns on disk structures that include thermal oxide on silicon and Bragg dielectric stacks. The scaling mass sensitivity of the IL channel on oxide on silicon was measured to be 0.17 pg/mm. © 2007 Optical Society of America  
*OCIS codes:* 110.4190, 120.3180, 310.6860, 180.5810.

## 1. Interferometric Detection of Proteins

The study of biological materials bound to solid surfaces became a topic of intense interest after gene and protein arrays [1–4] were introduced. Because a solid surface provides a visible and stable platform for multiplexed biomaterial interaction, with ample surface area for small spots, high through-put assays are possible on a microarray. To observe and record biochemical interactions on a solid platform, a fast and robust transduction is needed that converts molecular binding into an analytical signal. The traditional detection technique on arrays has been fluorescence, but this has limitations because of its reliance on fluorophores. Alternatively, many nonfluorescent techniques have been developed such as surface plasmon resonance [5–7], ellipsometry [8–10], thin-film interference [11,12], diffractometry [13,14], and waveguides [15]. These techniques have the advantage of requiring no fluorescent labels, but in exchange rely on detailed surface structuring or fabrication under

tight constraints or high incidence angles. These approaches seek to increase the signal-to-noise ratio (SNR) by increasing the signal, either through resonance or through increasing the electromagnetic interaction lengths.

We take the opposite approach to increase signal-to-noise performance by reducing noise. The principal means to accomplish this noise reduction is to spin the biosensor. This has the immediate result that the detection is moved from dc to high frequency with a significant suppression of the  $1/f$  noise. Typical noise suppression through spinning detection is 40 to 50 dB [16]. Therefore, our approach relies on no optical gain, making the sensor fabrication extremely simple: it removes fabrication-based contributions to noise, while relying entirely on the high-frequency detection to suppress the noise floor of the detection. Our detection mode is interferometry, which at high frequency is capable of detecting surface height changes below a picometer [17].

Based on this principle, we introduced spinning-disk interferometry (SDI) on bio-optical compact disk (BioCD) supporting monolayer or submonolayer proteins. The interferometry is performed in phase quadrature as common-path configurations that lock

the relative phase between the signal and the reference wave to  $90^\circ$ . The condition of phase quadrature provides the maximum transduction of phase (caused by the interaction of the field with the molecular dipoles) to intensity. In our case of two-field interference, the quadrature condition provides an optical gain of unity. Several different quadrature conditions have been explored for the BioCD including micro-diffraction [18], adaptive optics [19], phase contrast [20], and in-line (IL) [16]. The last two quadrature conditions were introduced as separate and independent detection modes, requiring different disk structures for optimization.

In this paper, we demonstrate that the phase-contrast and IL quadratures are, in fact, orthogonal quadratures of a single system response to the presence of protein on the disk. They carry complementary information about the protein profiles. For instance, the phase-contrast channel is sensitive to the spatial slopes of the protein layers, while the IL channel is sensitive to the protein height. The phase-contrast channel detects the asymmetric component of the far-field diffraction, while the IL channel detects the symmetric component. When the phase-contrast channel is maximum, the IL channel signal vanishes. Hence, by combining both channels, a stable signal may be obtained from virtually any substrate.

There have been reports of reflectance measurements to detect a protein layer on quasi-zero-reflection substrates [21,22]. These methods are related to the IL channel that we discuss here, but low reflectance is not essential to enhance the detection limit. For instance, as we will show, a surface with  $r = 0.58i$  reflectivity is preferred. Moreover, the phase-contrast channel obtains the phase change upon reflection, which cannot be acquired by reflectance measurements directly. Ellipsometry, likewise, shares much of the physics of the approach we describe here. However, our approach can operate surface-normal and is independent of polarization.

We describe the unified theory of the phase-contrast and IL channels in Section 2, where we derive the effect of a thin biolayer added on the top of a surface of arbitrary reflectivity. In the thin-film limit, the biolayer simply adds an incremental complex-valued contribution to the reflected field from the original surface. This limit is equivalent to the first Born approximation. Following this derivation, we show how the reflected phase and amplitude induced by the biolayer on any arbitrary surface may be extracted from the far field simply by adjusting the parity of the detector function. The experimental details of the disk structure and protein immobilization are presented in Section 3. We explore two types of disks: a Bragg dielectric stack and a thermal oxide on silicon. The Bragg stack is studied in the sidebands where the amplitude and phase vary rapidly with changing wavelength. In the case of thermal oxide, three different oxide thicknesses are investigated that separately optimize either the IL or the phase-contrast channels. The protein immobilization used

for this paper relied on the physical adsorption of silanized silica surfaces.

The optical detection system is described in Section 4, and the experimental results on the different varieties of disk are presented in Section 5. Comparisons of the experimental signal strengths are made to theory, with good agreement. The key distinction between SNR and signal-to-background ratio (SBR) is illustrated by comparing the signal power spectra of the different channels from different disks relative with the system noise. The phase-contrast channel has a clear advantage over the in-line channel in terms of SNR, because the differential far-field detection automatically compensates for common intensity drifts in the signal and reference waves. However, the IL channel has the advantage of direct protein detection. The two channels are therefore seen to provide complementary information about the protein as well complementary practical advantages.

## 2. Surface-Normal Protein Interferometry

Molecular interferometry on the BioCD is performed at angles of incidence that are surface-normal or nearly so. The probe beam is focused onto the disk surface in a single optical mode. Light diffracted or reflected from this single mode constitutes both the signal and the reference waves that combine in the far field to convert phase modulation (from spatially varying protein patterns) into intensity modulation at the detector. This section describes the two complementary quadrature conditions that lead either to differential phase-contrast detection or to IL detection. The signals in these two channels depend on the surface electromagnetic boundary conditions, the symmetry of the immobilized or surface-bound protein patterns, and the symmetry of the far-field detection.

The origin of the term “in-line” comes from an analogy with a thin layer that is in the optical path that provides a reference surface. When the layer is  $1/8$  wavelength thick, the partial reflections from the top and the bottom surfaces of the layer are in phase quadrature, which directly converts a phase modulation on the top surface into an intensity modulation. In this case, the bottom surface becomes the reference surface that is IL with the top sensor surface. This configuration is common-path, and hence is highly stable because of the rigidity of the layer. However, an IL structure is sufficient but not necessary to generate the IL channel. All that is required is a complex-valued reflectivity of the substrate that is purely imaginary. While the  $1/8$  wavelength layer is one way to accomplish this, other more complicated substrate structures also can achieve this phase condition, such as in the sidebands of a Bragg stack, which are discussed in Subsection 5.A.

### A. Protein on a Surface

A protein layer on a surface modifies the reflected amplitude and phase relative to the original surface. If the protein layer is treated as an extra dielectric layer on the underlying structure, then the transfer

matrix method [23] can be used to find the new Fresnel reflection coefficient as a function of the coefficient of the original substrate in the absence of the protein layer. When the protein layer is added on top of the substrate, the matrix product is

$$\begin{bmatrix} A' & B' \\ C' & D' \end{bmatrix} = \begin{bmatrix} e^{-i\delta_0} & r_p e^{-i\delta_0} \\ r_p e^{i\delta_0} & e^{i\delta_0} \end{bmatrix} \begin{bmatrix} e^{i\delta_p} & -r_p e^{i\delta_p} \\ -r_p e^{-i\delta_p} & e^{-i\delta_p} \end{bmatrix} \begin{bmatrix} A & B \\ C & D \end{bmatrix}, \quad (1)$$

where the primed coefficients refer to the protein-modified values,  $n_0$  is the refractive index of the incident medium,  $n_p$  is the refractive index of the protein layer,  $d$  is the layer thickness,  $\theta_0$  and  $\theta_p$  are the incident angle and refraction angle in the protein layer,  $\lambda$  is the wavelength of the probe light, and  $r_p$  is the reflection coefficient of the air-protein interface. For example, for  $s$ -polarization light the reflectivity is

$$r_p = \frac{\sin(\theta_p - \theta_0)}{\sin(\theta_p + \theta_0)}.$$

We use  $\delta_{0,p}$  to denote the phase change in the medium or the protein layer, respectively,

$$\delta_{0,p} = \frac{2\pi n_{0,p} \cos \theta_{0,p}}{\lambda} d.$$

Before the addition of the protein layer, the reflection coefficient is  $r = C/A$ , and after the addition it is  $r' = C'/A'$ . The new Fresnel reflection coefficient  $r'$  is related to the original substrate coefficient  $r$  through the expression

$$r' = \frac{(e^{i\delta_p} - e^{-i\delta_p})r_p + r(e^{-i\delta_p} - r_p^2 e^{i\delta_p})}{(e^{i\delta_p} - r_p^2 e^{-i\delta_p}) + r(e^{-i\delta_p} - e^{i\delta_p})r_p} e^{[2i(\tan \theta_p)/(\tan \theta_0)\delta_p]}. \quad (2)$$

According to this equation,  $r'$  is determined only by  $r$  and  $\delta_p$ , and has no explicit dependence on the details of the substrate structure. The information about the protein layer thickness is contained entirely in  $\delta_p$ .

When the protein is assumed to be a monolayer or less in thickness, Eq. (2) is expanded to give

$$r' = r + iP(r)\delta_p, \quad (3)$$

where  $P(r)$  is

$$P(r) = 2 \frac{(r_p - r)(1 - rr_p)}{(1 - r_p^2)} + 2r \left( \frac{\tan \theta_p}{\tan \theta_0} \right). \quad (4)$$

Equation (3) has the simple interpretation of a reference wave reflected with the original reflection coefficient of the bare substrate, added to a signal wave with a phase that is linearly dependent on the phase information of the protein layer. For a typical reflectivity of protein on a homogeneous dielectric support (such as silicon), the function  $P(r)$  is mostly real. If  $r$  is purely real and positive, then the protein produces net phase modulation when the two waves are combined in the far field. If  $r$  is purely imaginary, then the protein produces net intensity modulation when

the two waves are combined in the far field. In the general case of  $r$  neither purely real nor imaginary, then both effects occur together.

The detection of net phase modulation in the far field is achieved using an asymmetric detector function that is typically accomplished with a split detector and an inverting amplifier and summation circuit. The detection of net intensity modulation in the far field is achieved using a symmetric detector that simply detects the intensity. The next subsection describes these two complementary detection modes as simply the symmetric and antisymmetric parts of the far-field diffraction caused by the spatially varying protein on the substrate surface that has, in general, a complex value of reflectivity.

## B. Optical Diffraction

In the theoretical derivation of the common-path interferometric detection of protein, we consider both interference and diffraction upon reflection from the substrate, and we assume detection on the Fourier plane. We start with a reflecting planar substrate that has a complex reflection coefficient  $r$  carrying a protein layer of thickness  $h(x)$ . The boundary conditions for the surface uniquely determine the reflected amplitude and phase. The dimensionless electric field of the incident Gaussian beam is

$$g(\rho) = g(x, y) = \frac{1}{\sigma\sqrt{\pi}} e^{-(\rho^2/2\sigma^2)}, \quad (5)$$

with the two-dimensional Fourier transform

$$G(k_x, k_y) = \sigma\sqrt{\pi} e^{-2\sigma^2 k^2}. \quad (6)$$

The corresponding normalized two-dimensional intensity distribution is

$$I(\rho) = \frac{1}{\pi\sigma^2} e^{-\rho^2/\sigma^2},$$

where  $\rho^2 = x^2 + y^2$ ,  $\sigma = (\sqrt{2}/2)w_0$ , and  $w_0$  is the focal spot radius.

The two-dimensional diffraction problem is considered in the Fraunhofer regime. The reflected near field is

$$\begin{aligned} E(x, y) &= r'(x, y)g(x, y) \\ &= [r + iP(r)\delta_p]g(x, y) \\ &= \left[ r + iP(r) \frac{2\pi n_p h(x - vt, y) \cos \theta_0}{\lambda} \right] g(x, y) \\ &= r[1 + i\phi(r)h(x - vt, y)]g(x, y), \end{aligned} \quad (7)$$

where

$$\begin{aligned} \phi(r) &= \frac{P(r)}{r} \frac{2\pi n_p \cos \theta_p}{\lambda} \\ &= \left[ \frac{(r_p - r)(1 - rr_p)}{r(1 - r_p^2)} + \frac{\tan \theta_p}{\tan \theta_0} \right] \frac{4\pi n_p \cos \theta_p}{\lambda}. \end{aligned} \quad (8)$$

The surface topology, including the motion of the disk, is contained in the real-valued height function  $h(x + \eta, y)$ , here  $\eta = -vt$ , and  $v$  is the linear speed of the disk at the radius of the probe beam. The far field is

$$E(k_x, k_y) = r\{G(k_x, k_y) + i\phi(r)\text{FT}[g(x, y)h(x + \eta, y)]\}, \quad (9)$$

where FT denotes the Fourier transform. This equation describes the reflected far-field electric field when the laser beam is focused at position  $\eta$  of the protein profile.

For a nodal boundary condition, where  $r = -1$ , the value of  $\phi(r)$  in Eq. (8) at normal incidence is  $\phi(r) = 0$ . This has the initially surprising consequence that a biofilm on a nodal surface causes no amplitude and no phase shift and hence is effectively “invisible.” This is because on a perfect nodal surface the electric field is zero and so there is no molecular scattering, which is the origin of phase shifts and refractive indexes. On the other hand, for an ideal antinodal surface, where  $r = 1$ , the phase shift takes on a maximum value. These limiting cases are

$$\phi(r) = \begin{cases} 0 & \text{nodal} \\ \frac{4\pi(1 - n_p^2)}{\lambda} & \text{antinodal} \end{cases}, \quad (10)$$

with general substrates having values between these extremes.

The intensity at the detection (Fourier) plane is

$$\begin{aligned} I(k_x, k_y; \eta) &= |r\{G(k_x, k_y) + i\phi(r)\text{FT}[g(x, y) \\ &\quad \times h(x + \eta, y)]\}|^2 \\ &\approx |r|^2\{|G(k_x, k_y)|^2 \\ &\quad - 2G(k_x, k_y)\text{Im}[\text{FT}(\phi(r)g(x, y) \\ &\quad \times h(x + \eta, y))]\}. \end{aligned} \quad (11)$$

Because all protein profile information is included in the latter term, we neglect the dc part  $|G(k_x, k_y)|^2$  in the following discussion. The detected photocurrent is obtained by integrating Eq. (11) over the Fourier-plane detector response function  $R(k_x, k_y)$  that can be controlled by appropriate apertures or split detectors. The normalized photocurrent is

$$\begin{aligned} i_d(\eta) &= \int_{-\infty}^{\infty} R(k_x, k_y)I(k_x, k_y, \eta)d^2k \\ &= -2|r|^2 \int_{-\infty}^{\infty} R(k_x)G(k_x)\text{Im}[\phi\text{FT}(g(x) \\ &\quad \times h(x + \eta))]dk_x, \end{aligned} \quad (12)$$

where the second line is obtained by restricting the problem to the one-dimensional case. The IL signal is acquired by the summation of all reflected probe

light, while the differential phase-contrast (DPC) signal in the  $x$  direction is obtained using a split detector with inversion and summing circuits. The detector response function is

$$R(k_x) = \begin{cases} 1 & \text{for IL channel} \\ \text{sgn}(x) & \text{for DPC channel} \end{cases}$$

Both  $R(k_x)$  and  $G(k_x)$  are real functions, and  $\phi$  is a constant dependent only on the substrate properties. Therefore

$$\begin{aligned} i_d(\eta) &= -2|r|^2\text{Im}\left\{\phi \int_{-\infty}^{\infty} R(k_x)G(k_x)\text{FT} \right. \\ &\quad \left. \times [g(x)h(x + \eta)]dk_x\right\}. \end{aligned}$$

We introduce the function  $s(x)$ , where  $\text{FT}[s(x)] = R(k_x)$  and

$$s(x) = \begin{cases} \sqrt{2\pi}\delta(x) & \text{for IL channel} \\ i\sqrt{\frac{2}{\pi}}\frac{1}{x} & \text{for DPC channel} \end{cases} \quad (13)$$

Therefore

$$\begin{aligned} i(\eta) &= -2\frac{|r|^2}{2\pi}\text{Im}\left\{\phi \int_{-\infty}^{\infty} \text{FT}[s(x) \otimes g(x) \otimes (g(x) \right. \\ &\quad \left. \times h(x + \eta))]dk_x\right\}, \\ &= -2\frac{|r|^2}{\sqrt{2\pi}}\text{Im}\{\phi[s(x) \otimes g(x) \otimes (g(x)h(x + \eta))]|_{x=0}\}, \end{aligned} \quad (14)$$

and the two different detector output currents are now proportional to the quantities

$$\begin{aligned} i_d^{\text{IL}}(\eta) &= -2|r|^2\text{Im}\{\phi[g(x) \otimes (g(x)h(x + \eta))]|_{x=0}\}, \\ i_d^{\text{DPC}}(\eta) &= -2|r|^2\text{Im}\{i\phi[d(x) \otimes (g(x)h(x + \eta))]|_{x=0}\}, \end{aligned} \quad (15)$$

where  $d(x)$  is a Dawson function (Hilbert transformation of  $g(x)$ , which is an asymmetric function).

From Eq. (15)

$$\begin{aligned} i_d^{\text{IL}}(\eta) &= -2|r|^2\text{Im}\{\phi[g(x) \otimes (g(x)h(x + \eta))]|_{x=0}\}, \\ &= -2|r|^2\text{Im}\left\{\phi \int_{-\infty}^{+\infty} g(0 - \tau)g(\tau)h(\tau + \eta)d\tau\right\}, \\ &= 2|r|^2\phi_{\text{Im}}g^2(\eta) \otimes h(\eta). \end{aligned}$$

In a similar manner, the DPC channel of Eq. (15) is simplified into

$$i^{\text{DPC}}(\eta) = -2\phi_{\text{Re}} |r|^2 [(dg) \otimes h].$$

Replacing  $\eta$  with  $x$  gives

$$i^{\text{IL}}(x) = -2\phi_{\text{Im}} |r|^2 [g^2(x) \otimes h(x)],$$

$$i^{\text{DPC}}(x) = -2\phi_{\text{Re}} |r|^2 [(d(x)g(x)) \otimes h(x)], \quad (16)$$

where

$$\phi_{\text{Re}} = \frac{4\pi n_p \cos \theta_0}{\lambda} \text{Re} \left( \frac{(r_p - r)(1 - rr_p)}{r(1 - r_p^2)} + \frac{\tan \theta_p}{\tan \theta_0} \right),$$

$$\phi_{\text{Im}} = \frac{4\pi n_p \cos \theta_0}{\lambda} \text{Im} \left( \frac{(r_p - r)(1 - rr_p)}{r(1 - r_p^2)} \right). \quad (17)$$

Equation (16) is the exact simplified form of Eq. (12). They illustrate IL and DPC signals responding to local modulation of the Gaussian beam caused by a thin patterned biolayer on the dielectric surface. Explicitly, the IL channel sensitivity is determined only by the imaginary part of the conversion factor  $\phi(r)$ , while the DPC channel is determined only by the real part. With a knowledge of  $\phi(r)$  and the beam function  $g(x)$ , and by deconvolution, one can obtain the biolayer profile from any single channel. Therefore, both channels are capable of mapping the biomaterial topology on the BioCD. The key parameter that decides which channel has better sensitivity is  $\phi(r)$ . Because  $\phi(r)$  is a function of  $r$ , a specific dielectric stack design can maximize  $\phi_{\text{Im}}$  or  $\phi_{\text{Re}}$  to enhance the IL or the DPC channel, respectively.

Obviously, when  $r \rightarrow 0$ ,  $\phi_{\text{Im}}$  and  $\phi_{\text{Re}}$  both go to infinity. This explains why a quasi-zero-reflectance substrate greatly enhances the reflectance increment ratio due to the biomaterial layer. However, if  $r \rightarrow 0$ , the reflected light intensity is weak, and maintaining quasi-zero-reflectance tends to be unstable. Roughness of the substrate also plays a significant role in that it affects measurement precision and introduces noise. Therefore, in practical applications, the SNR is favored by maximizing  $\phi_{\text{Im}} |r|^2$ ,  $\phi_{\text{Re}} |r|^2$  instead of  $\phi_{\text{Im}}$  and  $\phi_{\text{Re}}$ . Calculations show that  $\phi_{\text{Im}} |r|^2$  reaches an extrema of  $\pm 0.0027$  (IL channel optimized) when  $r = \pm 0.58i$ , and  $\phi_{\text{Re}} |r|^2$  reaches an extrema of  $\pm 0.0272$  (DPC channel optimized) when  $r = 1$  (antinode disk). Here we assume that the incident angle is  $30^\circ$ , the wavelength is 488 nm and the refractive index of the biomaterial is 1.43.

The physical meaning of the DPC channel is somewhat elusive in Eq. (16). To obtain a more explicit equation, we perform an expansion of  $d(x)g(x)$  to obtain

$$d(x)g(x) = g(x)H(g(x)) = g^2(x) \sum_{n=0}^{\infty} \frac{(x/w_0)^{2n+1}}{(2n+1)n!}$$

$$= g^2(x)C(x),$$

$$= -0.5\sigma(g^2)^{(1)} - 0.04166\sigma^3(g^2)^{(3)}$$

$$- 0.003125\sigma^5(g^2)^{(5)} \dots \quad (18)$$

This expansion treats the polynomial  $C(x)$  as a vector and expands it in polynomials  $(g^2)^{(0)}/g^2 \sim (g^2)^{(n)}/g^2$ , where  $n$  denotes the  $n$ -order derivative. It can be shown that  $(g^2)^{(0)}/g^2 \sim (g^2)^{(n)}/g^2$  form a complete and nondegenerate polynomial vector space, so there is one and only one solution for the expansion.

Expanding gives

$$i^{\text{DPC}}(x) = -2\phi_{\text{Re}} |r|^2 [(d(x)g(x)) \otimes h(x)],$$

$$= -2\phi_{\text{Re}} |r|^2 \{ [-0.5\sigma(g^2)^{(1)} - 0.04166\sigma^3(g^2)^{(3)} \dots] \otimes h(x) \},$$

$$= 2\phi_{\text{Re}} |r|^2 \left[ 0.5\sigma g^2 \otimes \frac{dh}{dx} + 0.04166\sigma^3 g^2 \otimes \frac{d^3h}{dx^3} \dots \right].$$

The explicit equations for the IL and DPC channels are now

$$i^{\text{IL}}(x) = -2\phi_{\text{Im}} |r|^2 (g^2 \otimes h),$$

$$i^{\text{DPC}}(x) = 2\phi_{\text{Re}} |r|^2 \left[ 0.5\sigma g^2 \otimes \frac{dh}{dx} + 0.04167\sigma^3 g^2 \otimes \frac{d^3h}{dx^3} \dots \right]. \quad (19)$$

These relations show the clear separation between the two detection channels. DPC senses the differential protein height, being most sensitive to slopes and steps, while being insensitive to areas with uniform thickness. The far-field symmetry is antisymmetric, and the phase-contrast sensitivity is maximized when the reflectivity is real and positive (antinodal surface). The IL channel has the opposite attributes, sensing the direct protein height with a far-field that is symmetric, and the IL channel is maximized with a reflectivity that is purely imaginary. One way to achieve a purely imaginary substrate reflectivity is with a  $1/8$  wavelength layer, but other more complicated substrate structures can achieve this phase condition as well. For instance, a Bragg quarter-wave stack in the reflectance sideband achieves this condition for selected wavelengths, as described in Section 3.

Although Eqs. (16) and (19) are derived assuming one-dimensional protein topology, it is easy to generalize into two dimensions. For a protein pattern that is independent of the  $y$  axis (varies only in the  $x$

**Table 1. Refractive Index for the Relevant Dielectric Materials [32–34]**

	Air	SiO <sub>2</sub>	Ta <sub>2</sub> O <sub>5</sub>	Si	BSA Protein
488 nm	1.0	1.463	2.27	4.379 + 0.052i	1.43
633 nm	1.0	1.457	2.15	3.876 + 0.019i	1.43

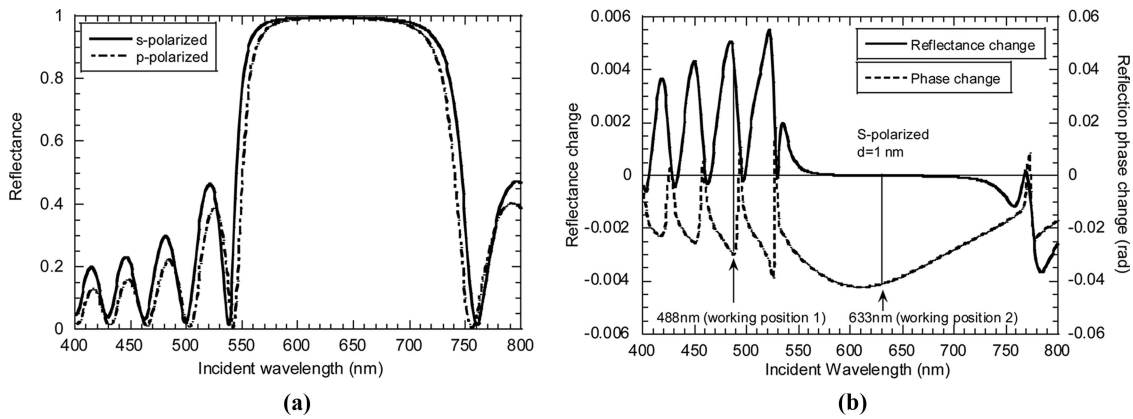


Fig. 1. (a) Calculated reflectance curves for a disk with a 20-layer Bragg stack for 30° incidence under *s*- and *p*-polarized light. (b) The reflectance and reflection phase changes when a 1 nm protein layer is applied on the Bragg stack disk for 30° incident *s*-polarization. The 633 and 488 nm probe wavelengths used in the experiments are indicated.

direction), Eqs. (16) and (19) accurately illustrate the two-channel signals of a two-dimensional pattern.

### 3. Disk Structures and Protein Immobilization

We have studied the two-channel interferometric response of proteins printed on two different types of disk structures. One is a high-reflectivity quarter-wave Bragg dielectric mirror with a center wavelength at 633 nm and a bandwidth of 200 nm. We detect the protein in the sideband region at a wavelength of 488 nm, where there are rapid shifts in the mirror reflectance as a function of wavelength or angle, and rapid shifts in reflected phase. The second structure is a simple thermal oxide on silicon. By choosing the oxide thickness or by changing wavelength, the two channels trade off continuously between each other.

#### A. Disk Structures

The quarter-wave dielectric Bragg stack has a center wavelength of 633 nm with a high reflectance larger than 99%. The surface layer is a 1/4 wavelength silicon dioxide layer that imposes an antinode condi-

tion ( $r = +1$ ) at the surface at the wavelength of 633 nm. The dielectric stack is composed of 20 quarter-wave dielectric layers on a glass substrate. The layers are  $\text{Ta}_2\text{O}_5$ , alternating with  $\text{SiO}_2$ , with layer thicknesses of 74 and 109 nm, respectively. The optical thickness of each layer is a quarter wave at 633 nm. The refractive indexes of the materials are given in Table 1. The calculated reflectance of the stack is shown in Fig. 1(a) at a 30° incidence for both *s* and *p* polarizations. The calculated changes in the reflectance and in the reflected phase in response to 1 nm of protein on the surface are shown in Fig. 1(b) for a 30° incident angle for *s*-polarized light. The reflectance and the phase vary rapidly as a function of wavelength, trading off against each other in a complementary manner. The reflectance change at 488 nm is predicted to be 0.0051/nm and phase modulation is predicted to be 0.031 radian/nm.

The second type of substrate is a single thermal oxide on a silicon wafer. Silicon has a refractive index at 633 nm of  $n = 3.876 + 0.019i$  and a reflectance of approximately 35%. The reflectance decreases as a thermal oxide is grown on the silicon until the reflectance

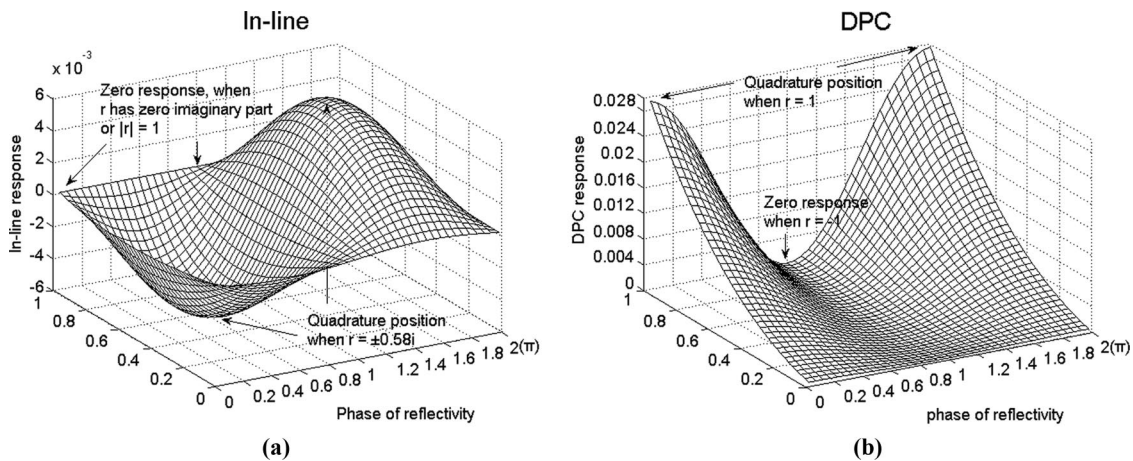


Fig. 2. (a) Calculated IL response and (b) DPC response to 1 nm protein layer as a function of the modulus and the phase of  $r$ . In the calculation, it is assumed that the incident angle is 30° (*s*-polarized) at a wavelength of 488 nm.

Table 2. Comparison between Theoretical and Experimental Results for the Ratio of Two-Channel Sensitivities

Disk Type	Theoretical Prediction of the Ratio DPC:IL		Experimental Result of the Ratio DPC:IL	
	At 488 nm	At 635 nm	At 488 nm	At 635 nm
80 nm silicon oxide	-1.63	-0.53	-2.11	-0.95
100 nm silicon oxide	1.32	-1.12	1.16	-1.50
120 nm silicon oxide	0.55	3.45	0.47	3.81
Antinode	0.40	$\infty$ (1:0)	0.44	$\infty$ (1:0)

tance reaches a minimum of 8.5% for a quarter-wave oxide thickness of 108 nm at a wavelength of 633 nm at normal incidence.

The nonnormalized ( $\Delta I$ ) DPC response and the IL response to 1 nm of protein are plotted as functions of the modulus and the phase of the reflectivity  $r$  in Figs. 2(a) and 2(b) for the IL and the DPC channels, respectively. From Fig. 2(a), the IL response is maximized at  $r = \mp 0.58i$ , and becomes null when  $r$  has zero imaginary part or when the modulus of  $r$  is 1. From Fig. 2(b), the DPC response is maximized at  $r = 1$  while null at  $r = -1$ . The orthogonal relation between the IL and the DPC responsivities is clear if the phase is changed at a constant modulus. The DPC responsivity curve is a cosine while the IL curve is a sine. The orthogonal relation can also be observed by fixing phase and changing the modulus.

#### B. Disk Protein Patterning

For protein immobilization we use physical adsorption based on methylation of the silica surface through treatment with chlorodimethyl-octadecylsilane ( $\text{CH}_3(\text{CH}_2)_{17}\text{Si}(\text{CH}_3)_2\text{Cl}$ ) that binds with silanol groups on the silica surface [24]. The  $\text{CH}_3$  endgroup of the silanes are hydrophobic and bind with protein through hydrophobic interaction. Hydrophobic interactions have large association constants and provide for a relatively simple means of immobilizing proteins on the disk surface [25,26]. The disks are soaked in 0.02 M chloro-octadecylsilane in toluene solution for 12 h and rinsed with toluene, acetone, methanol, and deionized water and dried with dry nitrogen gas. We print bovine serum albumin (BSA) (BSA-A9771, Sigma Corp.) protein in a grating pattern with the gel stamp method [27]. The gel stamp is fabricated by injecting liquid electrophoresis gel mixed with a protein solution into a mold that contains the grating pattern. After polymerization, the liquid gel becomes solid with a surface relief pattern that is used to print protein on the BioCD. After printing, the disk is rinsed with deionized water, and then blown dry with pure nitrogen. This procedure creates a monolayer (thickness is  $\sim 2.5$  nm) of immobilized protein in a stripe pattern with a protein stripe width of  $50 \mu\text{m}$  and a gap between the strips of  $100 \mu\text{m}$ . The thickness of the printed BSA has been calibrated against both adaptive interferometric metrology and atomic force microscopy [28], both of which confirm the monolayer character of the printed biolayer on this hydrophobic surface.

#### C. Theoretical Prediction for Two-Channel Sensitivity

We apply the theory to all four of the BioCD structures (Bragg stack, and thermal oxide on silicon with oxide thicknesses of 80, 100, and 120 nm) and calculate the two-channel sensitivities under the conditions of 488 and 633 nm laser illumination with a focal spot size of  $18 \mu\text{m}$ , and an incident angle of  $30^\circ$ . For the 100 nm oxide on silicon illuminated with the 488 nm argon laser, we calculate  $r = 0.27 - 0.24i$  (transfer matrix method) with  $\phi = -0.0295 - 0.011i$  [from Eq. (17)]. For the grating protein pattern, the thickness of the protein layer is assumed to be 1 nm. The amplitude ratio of the two channels is approximately based on computer simulation using Eq. (16). We also calculate the reflectivity and derive  $\phi_{\text{Re}}$ ,  $\phi_{\text{Im}}$ , and predict the two-channel amplitude ratios for all the BioCD structures, given in Table 2. The prediction of the signal amplitude ratios can be considered as the sensitivity ratio between the two channels.

#### 4. Optical Detection

The experiment is performed using two lasers with wavelengths of 633 and 488 nm, shown in the experimental layout in Fig. 3. These are incident at a  $30^\circ$  angle on the disk with the  $s$ -polarization. (The  $30^\circ$  angle is for convenience of the system setup, and is

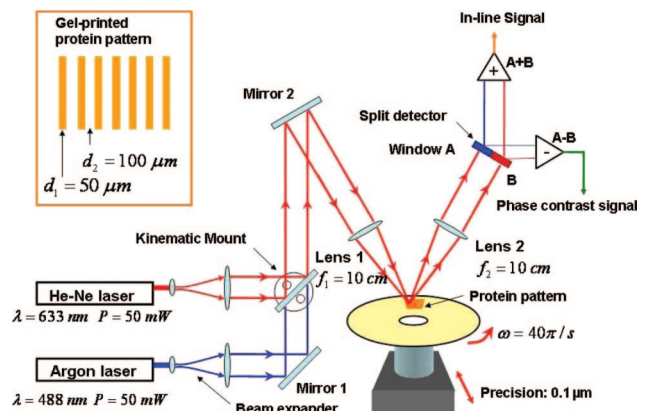


Fig. 3. Experimental layout using a He-Ne and an argon laser as light sources. The laser beam is incident at  $30^\circ$  and focused on the BioCD on a motor, which is fixed on a linear stage. The motor and stage create polar scanning coordinates. The diffracted signal is acquired by a split detector. By acquiring the sum and difference of the detector halves, we obtain the IL channel and DPC channel, respectively.

not fundamental. Surface-normal incidence works as well.) One laser is an INNOVA 300 laser (Coherent, Inc.) working at a wavelength of 488 nm. The other one is a helium–neon laser (Model 1248, Spectra-Physics) working at 633 nm wavelength. The two light sources are interchanged using a kinematic mount while keeping the light path unchanged. A 10 cm focal length convex lens is used to focus the laser beam onto the disk surface. The radius of the focal

spot is  $\sim 18 \mu\text{m}$  on the disk. Higher resolution can be achieved by switching the 10 cm lens with a short focal-length lens. Reflected light is guided into a quadrant detector that is responsible for acquiring the IL and phase-contrast signals. The split detector is divided into four quadrants. The left and right halves monitor the asymmetric far-field diffraction (phase-contrast channel), while the four-quadrant sum monitors the total light flux (IL channel). The

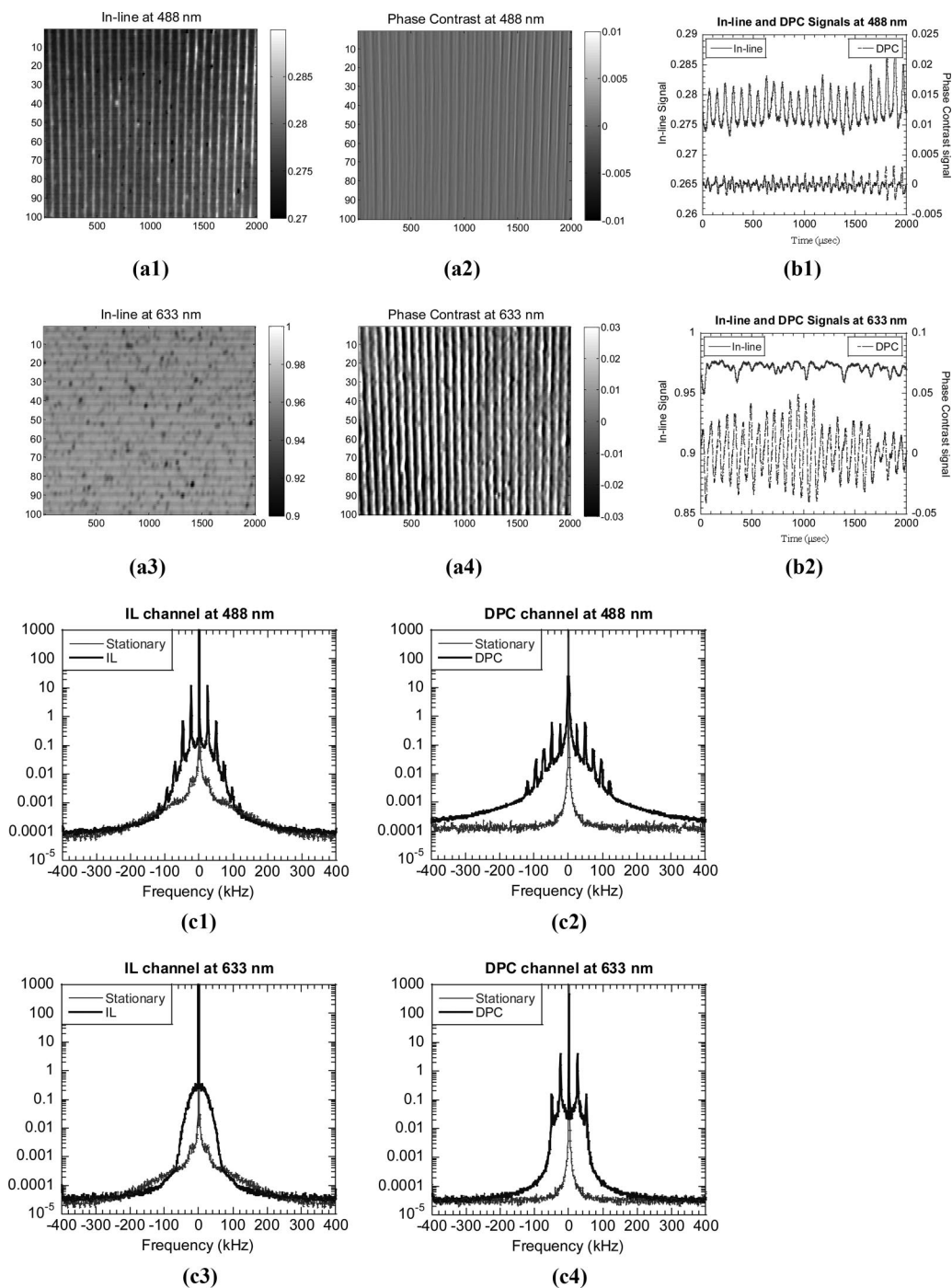


Fig. 4. Bragg stack BioCD illuminated at 488 and 633 nm wavelengths. At the 488 nm wavelength the IL and DPC signals share comparable amplitudes. At 633 nm the IL signal vanishes, and the DPC signal is maximum. The power spectra (c1)–(c4) are obtained from images (a1)–(a4).

split detector has a responsivity of 0.2 A/W for the 488 nm wavelength and 0.4 A/W for the 633 nm wavelength. The NEP is 0.63 nW/Hz<sup>1/2</sup>. The detector background noise is 8.3 μW.

The BioCD is positioned on a motor (Lincoln Laser, Inc.), which spins in a selectable frequency ranging from 20 to 80 Hz. The motor is fixed on a linear translation stage (MM2000, Newport Corp) that can move back and forth with 0.1 μm linear precision and 300 mm maximum travel distance. The motor and

linear stage form a polar coordinate system so that two-dimensional mapping can be realized with appropriate computer control. In this paper, experiments were done at a 20 Hz spin speed and a 20 μm linear step.

An oscilloscope records waveforms from the IL and phase-contrast channels for every track. Each track is averaged nine times. A computer records all waveforms for every track while controlling the linear stage motion, and two-dimensional images are recon-

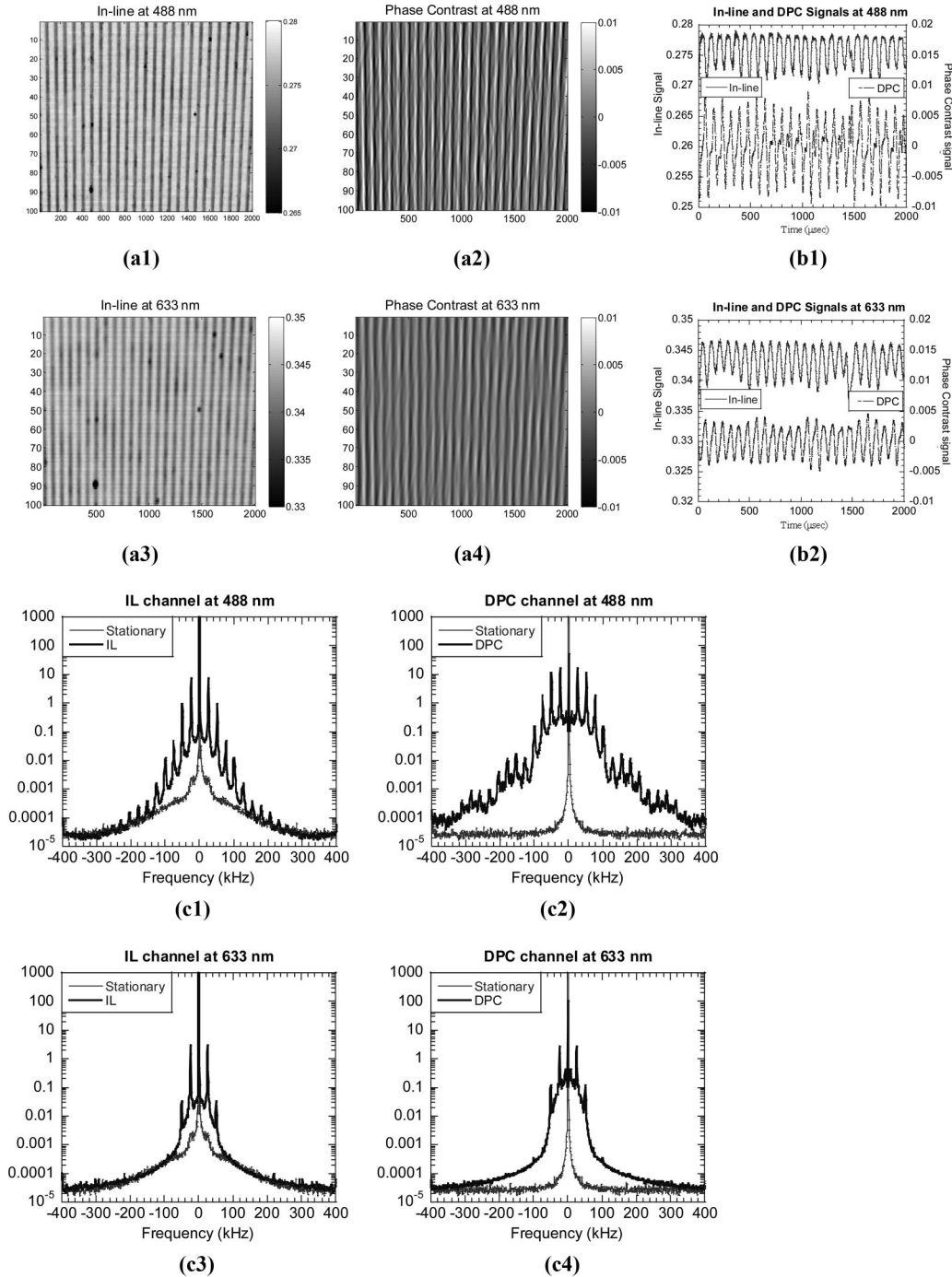


Fig. 5. 80 nm oxide on silicon illuminated at 488 and 633 nm wavelengths. These data show the area scans for IL and DPC channels (a1)–(a4) and the associated power spectra (c1)–(c4). Time traces for selected tracks are shown in (b1) and (b2).

structured with MATLAB software. This system is capable of mapping a 100 mm diameter BioCD in 30 min with 10 by 10  $\mu\text{m}$  pixel resolution.

### 5. Two-Channel Protein Interferometry on the BioCD

In this section we present the results of common-path interferometry of protein immobilized on the four types of substrates (Bragg stack, and three different oxide-on-silicon structures) detected at the two wave-

lengths of 488 and 633 nm in the two orthogonal channels using DPC and IL quadratures.

#### A. Dielectric Stack

We scanned a gel-printed 633 nm center-wavelength antinode disk using 488 and 633 nm laser wavelengths, respectively. The scanning area was 2 mm  $\times$  4 mm, shown in Figs. 4(a1)–4(a4). Under 633 nm illumination, the IL channel has no protein signal [Fig. 4(a3)] while the DPC channel [Fig. 4(a4)] has

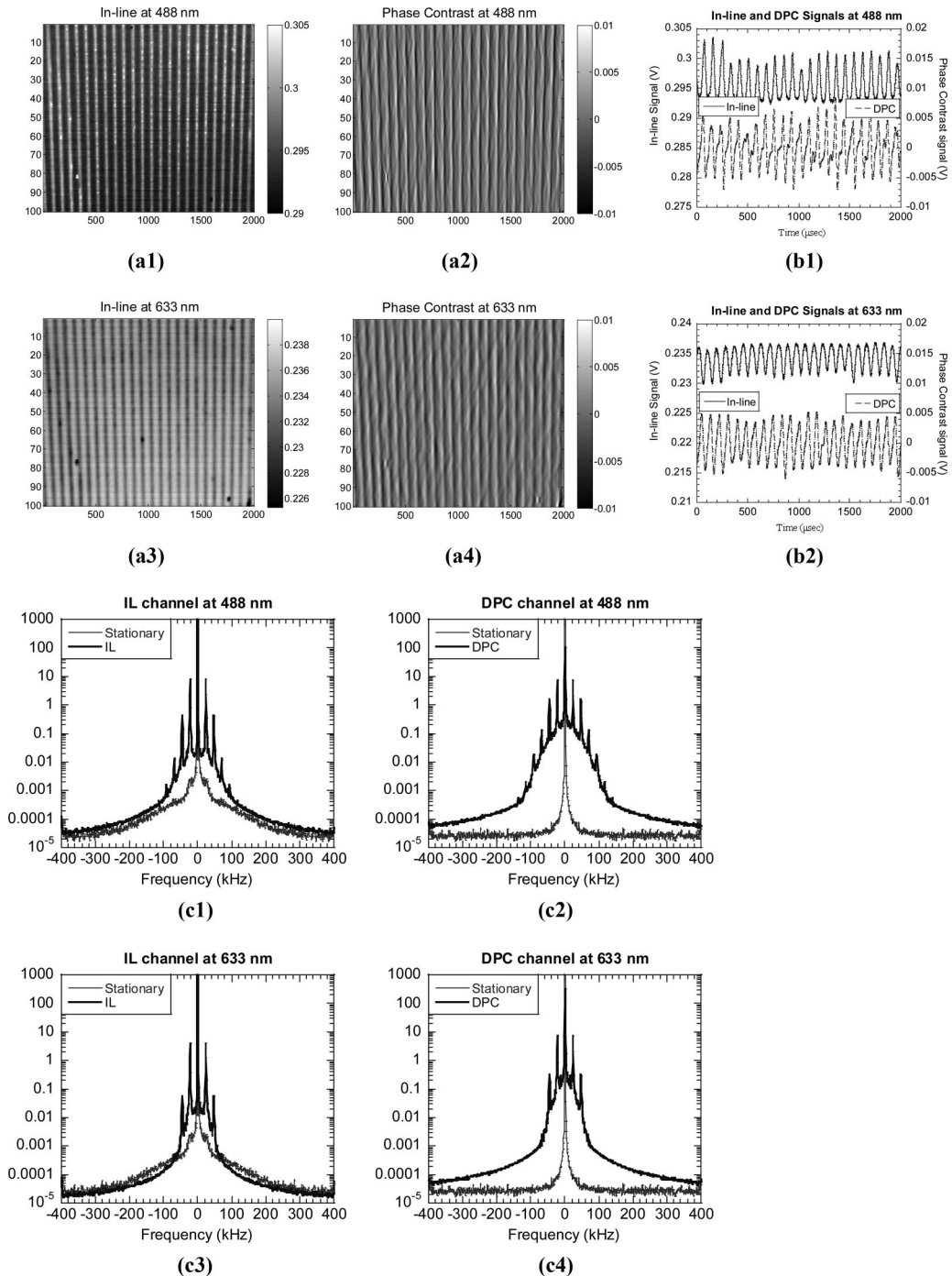


Fig. 6. 100 nm oxide-on-silicon disk illuminated at 488 and 633 nm wavelengths.

a strong signal. The dark spots in the IL image come from scattering by dust or particulates on the disk. They manifest themselves strongly when the reflectance of the disk is almost 100%. When the same disk was illuminated with the 488 nm laser wavelength, both channels had relatively strong signals. In Fig. 4(a1), the protein stripes in the IL channel are brighter than the background, indicating that the protein layer increases the reflectance of the BioCD.

To analyze the relative performance of the IL and the DPC signals, we extracted one track each (50th

from the DPC and IL images. These are shown in Figs. 4(b1) and 4(b2) (the  $y$  axis represents reflectance). Under 488 nm illumination, the amplitude ratio of the DPC to the IL channel is  $3.0 \times 10^{-3} : 6.8 \times 10^{-3} = 0.44$ . The theoretical value is  $1.6 \times 10^{-3} : 4.05 \times 10^{-3} = 0.40$  for a 1 nm protein layer. Therefore, the two-channel sensitivity ratio closely predicts the experimental results. The average thickness of the protein layer is calculated to be  $6.8 \times 10^{-3} / 4.05 \times 10^{-3} = 1.68$  nm.

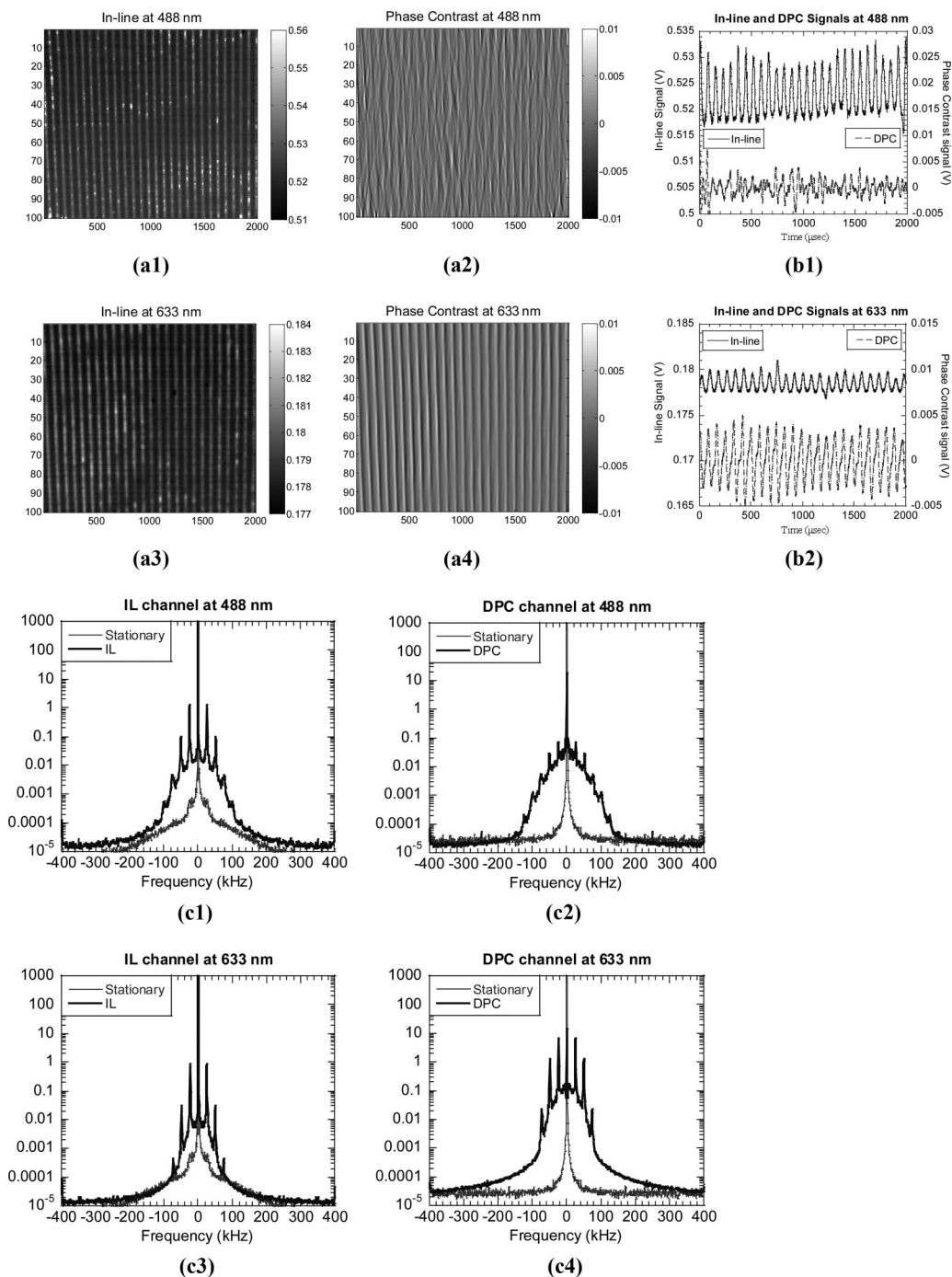


Fig. 7. 120 nm oxide-on-silicon disk illuminated at 488 and 633 nm wavelengths.

### B. Thermally Oxidized Silicon Wafer

We scanned gel-printed regions on the oxide-on-silicon disks with 80, 100, and 120 nm oxide thicknesses using 488 and 633 nm wavelengths, respectively. The scan area was 2 mm × 4 mm, as shown in Figs. 5–7. Both the wavelength and silica thickness affect the relative sensitivities of the IL and DPC channels. The protein layer decreases the 80 and 100 nm disk reflectance at the 633 nm wavelength, while it increases the 120 nm disk reflectance. At 488 nm, only the 80 nm disk exhibits a decrease in reflectance due to the protein layer, while for the 100 and 120 nm disks the reflectance increases with printed protein.

One track (50th) of each image is extracted and shown in Figs. 5(b1), 5(b2), 6(b1), 6(B2), and 7(b1) and 7(b2) (the y axis represents voltage of signal). There are six different working conditions (thickness of silica coating, incident wavelength). From these figures the ratios of the IL and DPC channel sensitivities are obtained by comparing the amplitudes of the two channels. (The amplitude of the DPC channel is the difference between the upper peak and lower peak.) The results are listed in Table 2. In the table, theoretical predictions and experimental results are listed for the ratio of the two-channel sensitivities. The negative sign on the ratio means that the protein layer decreases the disk reflectance. Figure 8 shows the IL and DPC channel sensitivities computed with the theory of Section 2. The experimental results of the sensitivities are also marked in Fig. 8. From Table 2 and Fig. 8, it is seen that theoretical predications agree well with the experimental results. The results have a relatively larger variation from predications at 633 nm illumination because of higher laser noise.

### C. Signal-to-Background Ratio and Signal-to-Noise Ratio

To calculate the detection limit of the IL and the DPC channels, we analyzed the power spectra of all images from Figs. 4–7 [29]. The analysis yields signal-

to-background ratio (SBR) and SNR values for each image. The SBR is obtained by calculating the intensity difference between the signal (the spikes in spectrum graph) and background near the signal. We distinguish SBR from SNR because the spectrum floor analyzed from the scan images is not actually noise, but is the disk roughness, which remains the same for every rotation and therefore is measurable and can be cancelled from the measurement. In Figs. 4(c1)–4(c4), 5(c1)–5(c4), 6(c1)–6(c4), and 7(c1)–7(c4), stationary (nonspinning) power spectra are presented, which are analyzed from the IL and DPC signals with all other conditions unchanged. These spectra consist of all noise sources except disk surface roughness. Therefore, they provide the noise floor. The SNR are used to denote the ratio of the signal intensity to the stationary spectrum floor. The SNR would equal the ideal SBR if the BioCD were perfectly smooth. The SNR represents the potential detection limit of the BioCD because the nonstochastic roughness that limits the SBR can be measured and removed from relative height changes caused by molecular binding on the BioCD surface.

In the low frequency region, the stationary IL and DPC spectra exhibit characteristics of  $1/f$  noise estimated as  $1/f^n$ . For the IL and DPC data in this paper, the transition from  $1/f$  noise to white noise is approximately 20 kHz. We spin the disk to shift the central frequency to higher frequencies than this one. Different protein patterns would demand different spinning frequencies. In the case of the gel-printed periodic pattern in this paper, the 20 Hz, disk frequency creates a 24 kHz signal frequency that is above the  $1/f$  noise region.

From the power spectrum of the Bragg disk [Fig. 4(c1)], the SBR = 173 in the 488 nm IL channel, while the SBR = 25 in the 488 nm DPC channel [Fig. 4(c2)]. The thickness of the protein layer was calculated to be 1.68 nm (the average thickness is 0.56 nm since only one-third of the area is covered by a protein

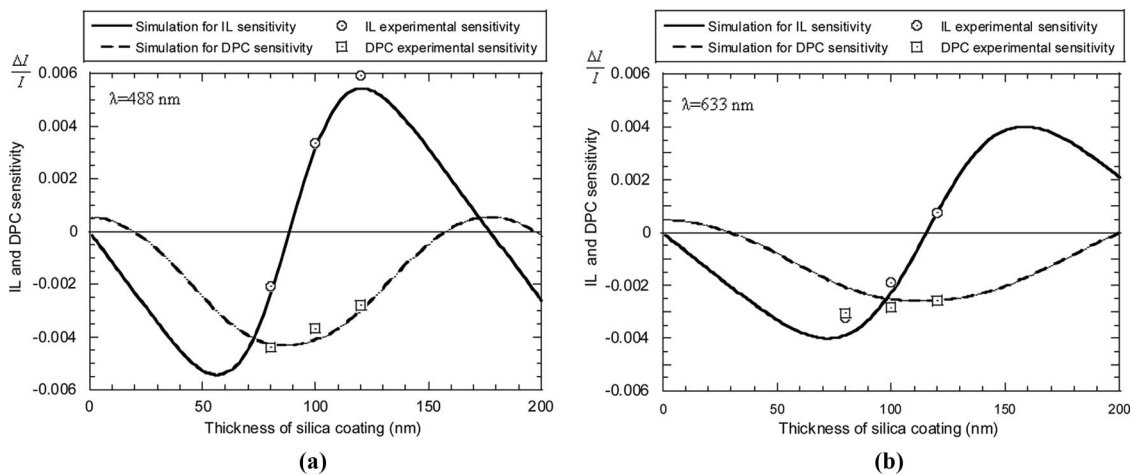


Fig. 8. IL and phase-contrast channel sensitivities for oxidized silicon wafers with different silica thicknesses. The curves are the theoretical simulations compared with experimental results.

Table 3. Experimental SBR and SNR Values (dB)

		80 nm Oxide Silicon Disk		100 nm Oxide Silicon Disk		120 nm Oxide Silicon Disk		633 nm Antinode Disk	
		SBR	SNR	SBR	SNR	SBR	SNR	SBR	SNR
488 nm	IL	22.90	34.38	28.63	38.63	20.17	32.79	22.38	33.26
	DPC	20.49	53.98	15.19	47.56	6.02	24.98	13.98	33.28
635 nm	IL	21.17	31.21	24.87	34.47	20.76	33.22	0.00	0.00
	DPC	15.31	44.77	18.39	47.85	20.09	49.49	18.63	46.53

layer) in Subsection 5.A. Therefore, the SBR = 173 in the IL channel, which sets the detection limit at 3.2 pm over the 8 mm<sup>2</sup> area (3.2 pg/mm<sup>2</sup> in traditional units), yielding a scaling mass sensitivity of  $\rho h \sqrt{A} = 9.0$  pg/mm (mass/area<sup>1/2</sup>) for the Bragg stack, where  $\rho$  is the density of protein (1 g/cm<sup>3</sup>),  $h$  is the detection limit of height, and  $A$  is the detection area. Here we adopt mass/area<sup>1/2</sup> as the sensitivity unit instead of the commonly used mass/area. This scaling is a consequence of data averaging for which the standard error is inversely proportional to the square root of the number of data samples [28]. The mass/area<sup>1/2</sup> is the intrinsic property of the detection system (it is an invariant value that is independent of the total area probed by the measurement), while mass/area is extrinsic (it varies with the size probed by the measurement). To make valid comparisons among many different detection systems that may rely on very different physical processes, it is necessary to use the intrinsic scaling sensitivities.

For all IL channels, the SNR is ~ten times larger than the SBR value. In Fig. 6(c1), the SBR = 7300 (SBR is ~730). The thickness of the protein layer was estimated as 1.33 nm (the average thickness is 0.44 nm since only one-third of the area is covered by a protein layer). This yields a scaling mass detection limit of 0.17 pg/mm (0.06 pg/mm<sup>2</sup> in traditional units on a 8 mm<sup>2</sup> area). We do not describe immunoassay experiments in this paper, concentrating exclusively on the detection physics of the two complementary interferometry channels, but this 0.17 pg/mm value measured here is in close agreement with the sensitivity measured for antigen-antibody immunoassays performed on BioCDs in prior work operating in the IL configuration [30], and in the phase-contrast configuration [31].

The DPC channel has more room for sensitivity improvement. In all of the power spectra of the DPC channels, the SNR is ~1000 times larger than the SBR. This is because the DPC signals are obtained from the difference of signals from the split halves of the same detector. Therefore, common-mode drifts in laser intensity can be compensated. The disk roughness and spinner vibration are the dominant noise sources for the DPC channel. With a smoother disk and a more stable spinner, the DPC detection limit could be improved to a large extent. The SBR and SNR for all experimental results are listed in Table 3.

## 6. Conclusions

This paper established the theoretical and experimental connection between the DPC channel and the IL common-path channels of the BioCD. The DPC signal arises from the antisymmetric far-field diffraction from the protein surface profile, while the IL signal arises from the symmetric far-field diffraction. The spatial response of the phase-contrast channel is proportional to the convolution of the probe beam shape with the first spatial derivative of the protein profile, while for the IL channel it is a direct convolution of the probe beam with the surface profile. The most striking connection between the phase-contrast and IL channels is in the continuous trade-off of signal between the two channels depending on the real and the imaginary part of the complex-valued reflectivity. We showed that a protein in the thin-layer limit contributes a scattered field to the bare-surface reflected field with a relative phase that is determined solely by the surface reflectivity. The details of the substrate structure are irrelevant in this analysis beyond what they contribute to the reflectivity. While an eight-wave layer on a uniform substrate (thermal oxide on silicon) is one way to establish phase quadrature between the original field and the contribution from the protein, many other structures are possible, for instance a Bragg stack in the sideband wavelengths.

We studied the relative sensitivities of the two channels on two types of disks, a dielectric Bragg stack with a 633 nm center wavelength, and thermal oxide on silicon. In the latter case, we studied three different oxide thicknesses that approximated the optimum conditions for phase-contrast detection, and two opposite quadrature conditions for the IL detection. In the IL channel in the optimal case of oxide on silicon, the SBR limits the scaling mass sensitivity to 2 pg/mm in terms of absolute measurements of surface mass density. However, the relative sensitivity, when comparing changes in mass density, is set by the SNR, which is larger by ~ an order of magnitude. Therefore, the relative sensitivity of the optimized IL channel is 0.2 pg/mm. This value agrees with values obtained previously in immunoassay experiments on the BioCD, and compares favorably with optimal sensitivities quoted for surface plasmon resonance detection that are typically 10 pg/mm<sup>2</sup> for commercial systems, which for state-of-the-art systems is 1 pg/mm<sup>2</sup> [7]. This introduction of simultaneous dual-channel common-path interferometry on the

BioCD makes the system highly versatile, capable of operating off of almost any substrate with any electromagnetic boundary conditions, while retaining high surface mass sensitivity.

This work was sponsored by grants from Quadraspec, Inc. and from the Indiana Economic Development Corporation through the Purdue Research Foundation.

## References

1. G. MacBeath and S. L. Schreiber, "Printing proteins as microarrays for high-throughput function determination," *Science* **289**, 1760–1763 (2000).
2. M. Schena, D. Shalon, R. Davis, and P. Brown, "Quantitative monitoring of gene-expression patterns with a complementary-DNA microarray," *Science* **270**, 467–470 (1995).
3. M. O'Brien, V. Perez-Luna, S. Brueck, and G. Lopez, "A surface plasmon resonance array biosensor based on spectroscopic imaging," *Biosens. Bioelectron.* **16**, 97–108 (2001).
4. C. Rowe, L. Tender, M. Feldstein, J. Golden, S. Scruggs, B. MacCraith, J. Cras, and F. Ligler, "Array biosensor for simultaneous identification of bacterial, viral, and protein analytes," *Anal. Chem.* **71**, 3846–3852 (1999).
5. B. Johnsson, S. Löfås, and G. Lindquist, "Immobilization of proteins to a carboxymethyl-dextran-modified gold surface for biospecific interaction analysis in surface-plasmon resonance sensors," *Anal. Chem.* **198**, 268–277 (1991).
6. U. Jonsson, L. Fagerstam, B. Ivarsson, B. Johnsson, R. Karlsson, K. Lundh, S. Lofas, B. Persson, H. Roos, I. Ronnberg, S. Sjolander, E. Stenberg, R. Stahlberg, C. Urbaniczky, H. Ostlin, and M. Malmqvist, "Real-time biospecific interaction analysis using surface-plasmon resonance and a sensor chip technology," *BioTechniques* **11**, 620–627 (1991).
7. J. Homola, S. Yee, and G. Gauglitz, "Surface plasmon resonance sensors: review," *Sens. Actuators B* **54**, 3–15 (1999).
8. M. Malmsten, "Ellipsometry studies of protein layers adsorbed at hydrophobic surfaces," *J. Colloid Interface Sci.* **166**, 333–342 (1994).
9. M. Landgren and B. Jonsson, "Determination of the optical properties of Si/SiO<sub>2</sub> surfaces by means of ellipsometry, using different ambient media," *J. Phys. Chem.* **97**, 1656–1660 (1993).
10. S. Lousinian and S. Logothetidis, "Optical properties of proteins and protein adsorption study," *Microelectron. Eng.* **84**, 479–485 (2007).
11. V. S. Y. Lin, K. Motesharei, K. P. S. Dancil, M. J. Sailor, and M. R. Ghadiri, "A porous silicon-based optical interferometric biosensor," *Science* **278**, 840–843 (1997).
12. K. P. S. Dancil, D. P. Greiner, and M. J. Sailor, "A porous silicon optical biosensor: detection of reversible binding of IgG to a protein A-modified surface," *J. Am. Chem. Soc.* **121**, 7925–7930 (1999).
13. L. Lading, J. A. Mann, and R. V. Edwards, "Analysis of a surface-scattering spectrometer," *J. Opt. Soc. Am. A* **6**, 1692–1701 (1989).
14. Y. G. Tsay, C. I. Lin, J. Lee, E. K. Gustafson, R. Appelqvist, P. Maggini, R. Norton, N. Teng, and D. Chariton, "Optical biosensor assay," *Clin. Chem.* **37**, 1502–1505 (1991).
15. N. Skivesen, A. Tetu, M. Kristensen, J. Kjems, L. H. Frandsen, and P. I. Borel, "Photonic-crystal waveguide biosensor," *Opt. Express* **15**, 3169–3176 (2007).
16. M. Zhao, X. Wang, and D. Nolte, "The in-line-quadrature bioCD," *Proc. SPIE* **6447**, 64470B (2007).
17. S. I. Stepanov, I. A. Sokolov, G. S. Trofimov, V. I. Vlad, D. Popa, and I. Apostol, "Measuring vibration amplitudes in the picometer range using moving light gratings in photoconductive GaAs-Cr," *Opt. Lett.* **15**, 1239–1241 (1990).
18. M. M. Varma and D. D. Nolte, "Spinning-disk self-referencing interferometry of antigen-antibody recognition," *Opt. Lett.* **29**, 950–952 (2004).
19. L. Peng, M. M. Varma, and D. D. Nolte, "The adaptive BioCD: interferometric immunoassay on a spinning disk," *Proc. SPIE* **5692**, 224–232 (2005).
20. M. Zhao and L. Peng, "Phase-contrast BioCD: high-speed immunoassays at subpicogram detection levels," *Proc. SPIE* **6095**, 93–104 (2006).
21. T. Gao, J. Lu, and L. J. Rothberg, "Biomolecular sensing using near-null single wavelength arrayed imaging reflectometry," *Anal. Chem.* **78**, 6622–6627 (2006).
22. H. Arwin and I. Lundstrom, "A reflectance method for quantification of immunological reactions on surfaces," *Anal. Biochem.* **145**, 106–112 (1985).
23. O. S. Heavens, *Optical Properties of Thin Solid Films* (Academic, 1955).
24. J. Duchet, B. Chabert, J. P. Chapel, J. F. Gerard, J. M. Chovelon, and N. Jaffrezic-Renaul, "Influence of the deposition process on the structure of grafted alkylsilane layers," *Langmuir* **13**, 2271–2278 (1997).
25. Z. H. Wang and G. Jin, "Silicon surface modification with a mixed silanes layer to proteins for biosensor with imaging ellipsometry," *Colloids Surf. B* **34**, 173–177 (2004).
26. N. B. Sheller and S. Petrash, "Atomic force microscopy and x-ray reflectivity studies of albumin adsorbed onto self-assembled monolayers of hexadecyltrichlorosilane," *Langmuir* **14**, 4535–4544 (1998).
27. B. D. Martin and B. P. Gaber, "Direct protein microarray fabrication using a hydrogel stamper," *Langmuir* **14**, 3971–3975 (1998).
28. L. L. Peng, M. M. Varma, F. E. Regnier, and D. D. Nolte, "Adaptive optical biocompact disk for molecular recognition," *Appl. Phys. Lett.* **86**, 183902 (2005).
29. J. W. Goodman, *Introduction to Fourier Optics* (McGraw-Hill, 1968).
30. D. D. Nolte and M. Zhao, "Scaling mass sensitivity of the BioCD at 0.25 pg/mm," *Proc. SPIE* **6380**, 63800J (2006).
31. M. Zhao, D. Nolte, W. R. Cho, F. Regnier, M. Varma, G. Lawrence, and J. Pasqua, "High-speed interferometric detection of label-free immunoassays on the biological compact disc," *Clin. Chem.* **52**, 2135–2140 (2006).
32. J. M. Albella, J. M. Martinez-Duart, and F. Rueda, "Index of refraction of tantalum oxide in the wavelength interval 2750–14000 Å," *Opt. Acta* **22**, 973–979 (1975).
33. H. Arwin, "Optical properties of thin layers of bovine serum albumin,  $\gamma$ -globulin, and hemoglobin," *Appl. Spectrosc.* **40**, 313–318 (1986).
34. D. E. Aspnes, *Properties of Silicon* (INSPEC, 1988).